# Perovskite oxide heterojunction for Rashba-Dresselhaus assisted antiferromagnetic spintronics

Jayita Chakraborty* and Nirmal Ganguli†

*Department of Physics, Indian Institute of Science Education and Research Bhopal, Bhauri, Bhopal 462066, India*

(Received 6 November 2020; accepted 7 December 2020; published 21 December 2020)

A major impediment towards realizing technologies based on the emerging principles of antiferromagnetic spintronics is the shortage of suitable materials. In this paper, we propose a design of polar|nonpolar heterostructures of perovskite oxides, where a single unit cell of $SrIrO_3$ is sandwiched between a thin film of $LaAlO_3$ and a substrate of $SrTiO_3$. Our calculations within the framework of density-functional theory + Hubbard $U$ + spin-orbit coupling reveal a two-dimensional conducting layer with electron and hole pockets at the interface, exhibiting a strong anisotropic Rashba-Dresselhaus effect along with noncollinear antiferromagnetism, indicating the possibility of realizing a spin-orbit torque. An insightful physical model for the anisotropic Rashba-Dresselhaus effect nicely interprets our results, providing an estimate for the Rashba-Dresselhaus coefficients and illustrating pseudospin orientation. We also observe a proximity-induced prominent Rashba-like effect for Ti 3$d$ empty bands. Our results suggest that the heterostructure may possess the essential ingredients for antiferromagnetic spintronics, deserving experimental verification.

DOI: 10.1103/PhysRevB.102.214425

## I. INTRODUCTION

The use of antiferromagnetic materials for spintronic applications has recently been identified as one of the most promising paths for future technology development [1–4]. Some of the advantages of antiferromagnetic materials over their conventional ferromagnetic counterparts include robustness against perturbation due to magnetic fields, the absence of stray fields, and ultrafast spin dynamics. Besides potentially facilitating ultrafast computational operations at a low energy cost, antiferromagnetic spintronic materials are promising for nonvolatile memory devices with a terahertz electrical writing speed [5]. Spin-orbit torque due to strong Rashba-like spin-orbit interaction may help manipulate the magnetic domains and antiferromagnetic spin textures [1]. Therefore, realizing a substantial Rashba-like effect in a two-dimensional conducting layer along with antiferromagnetism is one of the possible routes for further developments of antiferromagnetic spintronics.

Heterostructures of iridates hold a substantial promise in the lookout for suitable materials for realizing antiferromagnetic spintronics. The emerging research on iridates reveals fascinating physical properties, owing to the interplay of spin-orbit interaction, electron-electron correlation, and crystal-field splitting—all with comparable strength in these systems [6–8]. Moreover, heterostructures of iridates and other 5$d$ oxides may lead to a new paradigm where constraining the electron movement can trigger novel properties that are useful for technology [9–12]. In a pioneering work, Matsuno *et al.* [9] synthesized superlattices of $[(SrIrO_3)_m, SrTiO_3]$ using a pulsed-laser deposition technique and studied the physical properties. Their results point out that, besides being an insulator, Ir magnetic moments order over a long range in canted antiferromagnetic fashion in $SrIrO_3$ for $m = 1$, suggesting its similarity with the layered $Sr_2IrO_4$. The discussion indicates intuitively that an ultrathin film of $SrIrO_3$ deposited on a noninterfering substrate may mimic some of the physical properties of $Sr_2IrO_4$, owing to the interaction between Ir atoms along the $c$ direction being restricted. Another combined experimental and theoretical study suggests that the opening of a gap in an ultrathin film of $SrIrO_3$ requires antiferromagnetic order [10]. Thin films of $SrIrO_3$ may also exhibit spin-orbit torque [13,14]. However, a two-dimensional conducting system along with robust antiferromagnetism and a strong Rashba-like effect—a combination potentially useful for antiferromagnetic spintronics—has not yet been realized.

In this paper, we propose an ingenious way of realizing a two-dimensional conducting layer with strong spin-orbit interaction leading to the Rashba-Dresselhaus effect in an antiferromagnetic background crucial for hosting antiferromagnetic spintronics. We study a heterostructure having one unit cell of SIO sandwiched between a thick $TiO_2$-terminated $SrTiO_3$ (STO) substrate and a thin film of LaO-terminated $LaAlO_3$ (LAO) along the 001 direction. Having alternating $+1|-1$ charged planes along the 001 direction, LAO would lead to monotonic development of electric potential when deposited on a nonpolar material, causing electronic reconstruction [15]. Thus, the heterostructure of polar LAO with nonpolar $IrO_2$-terminated SIO|STO is expected to develop an n-type interface, where the carriers would be confined to the $IrO_2$ plane, resulting in a two-dimensional conducting layer at the interface. Since the band gap (Mott-like gap) of SIO is very small, an estimate of charge transfer similar to Ref. [15] would suggest that only a few-unit-

*Present address: Department of Physics, Vivekananda Satavarshiki Mahavidyalaya, Manikpara, Jhargram, WB721513, India; Jayita.Chakraborty1@gmail.com

†NGanguli@iiserb.ac.in

 

cell-thick LAO would be sufficient for transferring ≈0.5e per interface unit cell. Our investigation progresses as follows: first we simulate a $TiO_2$-terminated $(SrIrO_3)_1|(SrTiO_3)_1$ heterostructure and its $2 \times 2$ supercell in the *ab* plane (henceforth referred to as a $2a \times 2b$ cell) to analyze the electronic structure and magnetic properties. Subsequently, a $(LaAlO_3)_{2.5}|(SrIrO_3)_1|(SrTiO_3)_{4.5}$ heterostructure that ensures ≈0.5e per unit cell transfer to the n-type interface and its $2a \times 2b$ supercell are simulated. The electronic structure, magnetic properties, and spin-orbit interaction driven Rashba-like effects are thoroughly investigated for these heterostructures with the help of an analytical model. The remainder of the paper is organized as follows: The methodology of our calculations is described in Sec. II. A detailed discussion of our results is provided in Secs. III and IV. Finally, we summarize the work in Sec. V.

## II. METHOD

Although we aim at understanding the physical properties of a heterostructure with ultrathin films of SIO and LAO deposited on a thick STO substrate, here we simulate superlattices of $(SrIrO_3)_1|(SrTiO_3)_1$ and $(LaAlO_3)_{2.5}|(SrIrO_3)_1|(SrTiO_3)_{3.5}|(SrIrO_3)_1$ comprising n-type interfaces between LaO and $IrO_2$ planes, subject to periodic boundary conditions along every direction in order to capture the essential physics of the heterostructures within affordable computational cost. The choice of the fractional number of unit cells for the constituent materials ensures the transfer of 0.5 electrons per interface unit cell in order to satisfy the preferred oxidation states of the A-site cation and the oxygen anion. $2a \times 2b$ cells are simulated to accommodate tilted $IrO_6$ octahedra and various antiferromagnetic orders. All our calculations of total energy, electronic structure, and magnetic properties of SIO|STO and LAO|SIO|STO heterostructures are carried out using density-functional theory within a plane-wave basis set along with the projector augmented wave (PAW) method [16], as implemented in the VASP code [17,18]. The generalized gradient approximation (GGA) due to Perdew, Burke, and Ernzerhof (PBE) is used for the exchange-correlation functional [19]. Some of the key results were verified within the local density approximation (LDA) [20,21] for consistency. Strong Coulomb correlation in *d* and *f* orbitals was described within the DFT + Hubbard *U* (GGA + *U*) method [22], with $U - J = 2$, 1.5, and 10 eV for Ti $3d$, Ir $5d$, and La $4f$ states, respectively. The large *U* value for La $4f$ states ensure locating these empty states sufficiently high in energy to avoid any artifacts in the electronic structure arising from them. The Brillouin-zone integration is performed within an improved tetrahedron method [23] using a Γ-centered dense *k* mesh of $15 \times 15 \times 1$ for the three-dimensional bands and Fermi contour calculations, a $9 \times 9 \times 1$ mesh for the rest of the calculations involving $2a \times 2b$ cells, and a $19 \times 19 \times 1$ mesh for the calculations involving $1a \times 1b$ cells. The system's total energy was well converged to a threshold of $10^{-7}$ eV for the calculations considering spin-orbit interactions. Mimicking a possible epitaxial growth of the thin films of SIO and LAO on a thick substrate of STO, we constrain the lattice constant in the *ab* plane to match that of STO, allowing relaxation only along the *c* direction to minimize the stress. The atomic positions are optimized to minimize the Hellman-Feynman forces on each atom with a tolerance of 0.01 eV/Å.

## III. RESULTS

The results obtained from our calculations are discussed below.

### A. $SrIrO_3|SrTiO_3$

Since the SIO|STO heterostructure plays the role of a benchmark for our study of the LAO|SIO|STO heterostructure, carefully understanding the electronic structure and magnetic properties of SIO|STO is imperative for further progress. Below we discuss the results of our calculations with $(SrIrO_3)_1|(SrTiO_3)_1$ heterostructure. Because each Ir (Ti) atom is surrounded by six O atoms forming an octahedron, Ir $5d$ (Ti $3d$) spin-degenerate states split into a lower-energy threefold degenerate $t_{2g}$ manifold and a higher energy twofold degenerate $e_g$ manifold. Furthermore, strong spin-orbit interaction in an $Ir^{4+}$ ion splits the $t_{2g}$ manifold into a lower-energy completely filled $J_{\text{eff}} = 3/2$ quartet and a higher-energy half-filled $J_{\text{eff}} = 1/2$ doublet. Our results for the calculations with $1a \times 1b$ structure reveals the conducting nature of the heterostructure, owing to Ir $5d$ bands crossing the Fermi level. The band dispersion along the $X \rightarrow \Gamma \rightarrow M$ direction (the Brillouin-zone geometry has been discussed in Appendix A) and the density of states (DoS) are displayed in Figs. 1(a) and 1(b), respectively. We note that Ir $5d$ states, hybridized with O $2p$ states, constitute the states near the Fermi level ($E_F$). Ti $3d$ states in $Ti^{4+}$ ions are completely empty and lie above $E_F$. The heterostructure's metallic character originates from the Ir-$5d$–O-$2p$ hybridized states, suggesting that the conduction electrons are confined to the single layer of $SrIrO_3$, leading to a two-dimensional conducting layer. To allow antiferromagnetic order or tilted $IrO_6$ octahedra, we have simulated a $2a \times 2b$ supercell. In practice, a heterostructure with an ultrathin film of SIO grown on a thick substrate of STO would adapt to STO's lattice constant in the *ab* plane. On the other hand, the lattice constant along the *c* direction is unconstrained and governed by the Poisson ratio of the respective materials. When deposited on the STO substrate, SIO undergoes an in-plane compressive strain. The inset of Fig. 1(d) shows the optimized structure with tilted $IrO_6$ octahedra having a $a^0b^0c^-$ tilt pattern with reference to the nearby STO layer [24] and an angle of 14.1° about the *c* axis, in agreement with experiments [25–27]. Our calculations for a $2a \times 2b$ supercell, including spin-orbit interaction, suggest that a ferromagnetic order is not stable. We realize a weak canted antiferromagnetic arrangement, as depicted with arrows in the inset of Fig. 1(d), with projected spin and orbital magnetic moments of $0.12\mu_B$ and $0.27\mu_B$, respectively, at the Ir site. The band structure [Fig. 1(c)] and the density of states [Fig. 1(d)] corresponding to the antiferromagnetic phase clearly shows a small energy gap of 0.16 eV near the Fermi level. Such a band-gap opening, driven by antiferromagnetic order, with a moderate value of $U - J = 2$ eV within the GGA + *U* method suggests a Mott- or Slater-like insulating state of the monolayer of $SrIrO_3$, owing to the absence of interaction between Ir atoms along the *c* direction, similar

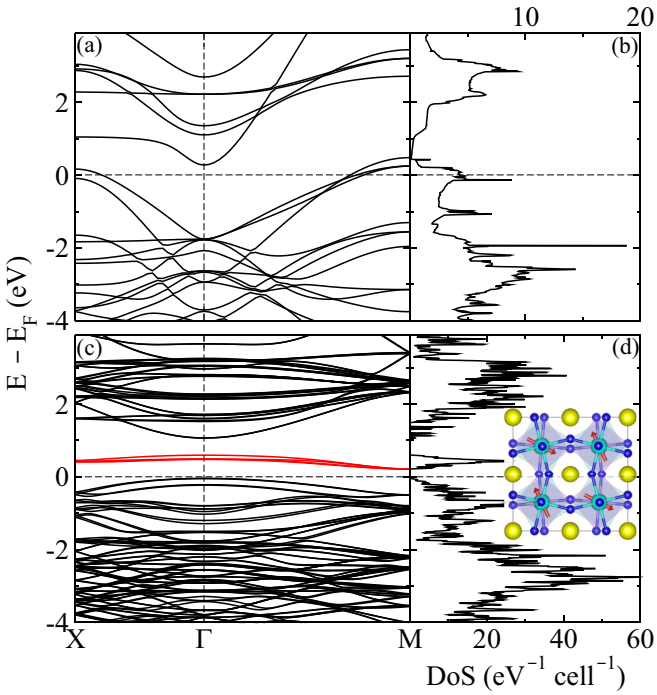


FIG. 1. The band structure along the X → Γ → M direction for SIO|STO with $1a \times 1b$ structure (spin-unpolarized) and with $2a \times 2b$ supercell (antiferromagnetic) with spin-orbit interaction are shown in panels (a) and (c), respectively. Panels (b) and (d) exhibit the density of states corresponding to panels (a) and (c), respectively. The inset of panel (d) depicts the tilted $IrO_6$ octahedra and a canted magnetic arrangement.

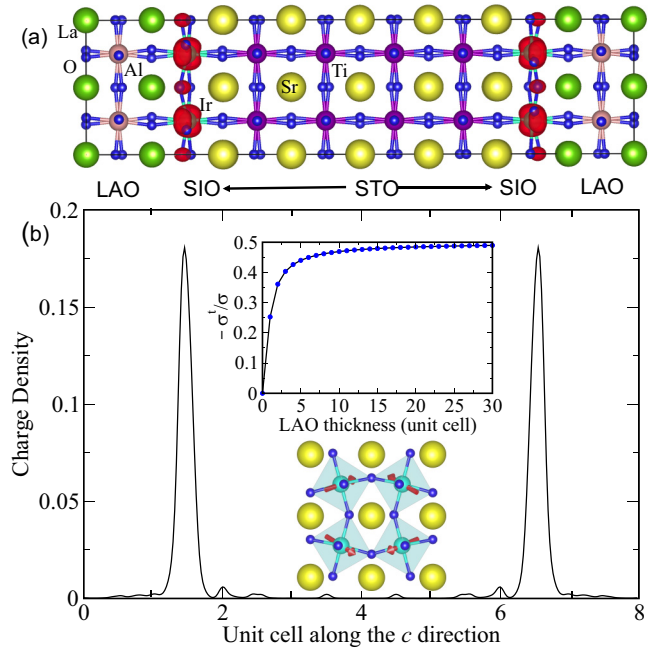


FIG. 2. Panel (a) depicts the transferred charge-density isosurfaces for the LAO|SIO|STO heterostructure, while panel (b) shows the transferred charge-density summed over the *ab* plane varying with the unit cells along the *c* direction. An electrostatic estimate of charge transfer as a function of $LaAlO_3$ thickness and an illustration of the tilted $IrO_6$ octahedra marking the magnetic moment vectors are given in the insets of panel (b).

to $Sr_2IrO_4$ [28,29]. Our results do not reveal any Rashba-like splitting of the bands, consistent with the experimental report of temperature-dependent weak Rashba-like effect for SIO|STO heterostructure (see Appendix B for further details) [30]. An isolated narrow (0.37 eV wide) $J_{\text{eff}} = 1/2$ band appears right above the Fermi level, which would lead to interesting physics upon charge transfer.

### B. $LaAlO_3|SrIrO_3|SrTiO_3$

Similar to the polar-nonpolar oxide heterostructure of LAO|STO, deposition of a thin film of the polar oxide LAO on the one-unit-cell-thick film of $IrO_2$-terminated nonpolar SIO grown on nonpolar STO substrate is expected to result in an n-type interface with the two-dimensional conducting layer being confined at the $IrO_2$ plane.

#### *1. Tilted* $IrO_6$ *octahedra*

We optimized the atomic positions and the lattice constant along the *c* direction for the simulated LAO|SIO|STO heterostructure, constraining the lattice constant in the *ab* plane to that of STO. An $a^0b^-c^-$ tilt pattern emerges from our calculations, with tilt angles of 5.4° and 13.4° about the *b* and *c* axes, respectively [see Figs. 2(a) and 2(b), inset], which lowers the total energy of the system by 0.45 eV per Ir atom when compared with a heterostructure without octahedral tilts. The enhanced tilts can further confine the electrons in the local orbitals, reinforcing magnetism [15]. We note that, in the absence of experiments, the possible thickness of a LAO film grown on an ultrathin film of SIO is not known. At this stage, an estimate of the charge transfer amount to the interface would help understand the proposed system's physical properties.

#### *2. Charge transfer*

Our estimate of charge transfer is based on electrostatics, as described in Ref. [15]. Using appropriate values for the parameters,[1] we obtained the ratio of the required amount of transferred surface charge density $\sigma^t$ to the surface charge density of a positively charged plane $\sigma$ for avoiding the polar catastrophe, as shown in the inset of Fig. 2(b). Because of the small Mott-like gap near the Fermi level and the small valence-band offset between $SrIrO_3$ and $LaAlO_3$, the required amount of transferred charge rapidly approaches its saturation value of $0.5e^-$ per interface unit cell with increasing thickness of LAO, reaching $0.4e^-$ for as thin as three unit cells of LAO. Hence we justify representing the arrangement of the thin films described above by simulating a LAO|SIO|STO heterostructure [see Fig. 2(a)] within periodic boundary conditions along the *c* direction, which ensures the transfer of $0.5e^-$ per interface unit cell.

The charge-density isosurface plot for the transferred charge displayed in Fig. 2(a) finds the transferred charge pop-

[1]We have used $\epsilon^{\text{LAO}}/\epsilon_0 = 24$, $\epsilon_0$ being the permittivity of free space, $\varepsilon_g + \Delta = 0.35$ eV, $K^{\text{IF}} = 0.5$ F$^{-1}$.

TABLE I. The spin (orbital) magnetic moment projected onto the Ir ions and the relative energies $\Delta E$ in meV for different magnetic configurations of LAO|SIO|STO: canted ferromagnetic (FM), canted checkerboard antiferromagnetic (CB-AFM), and canted striped antiferromagnetic (ST-AFM) are tabulated here.

| Configuration | $U - J = 1.5$ eV | | $U - J = 2.0$ eV | |
|---|---|---|---|---|
| | Ir moment ($\mu_B$) | $\Delta E$ | Ir moment ($\mu_B$) | $\Delta E$ |
| FM | 0.2 (0.21) | 0.85 | 0.21 (0.23) | 0.68 |
| CB-AFM | 0.2 (0.24) | 0.00 | 0.21 (0.25) | 0.00 |
| ST-AFM | 0.2 (0.24) | 0.53 | 0.21 (0.25) | 0.50 |

ulating the hybridized Ir-5$d$–O-2$p$ states in the $IrO_2$ plane. Furthermore, we calculated the transferred charge density $\rho(z)$ within the appropriate energy range, summing over the FFT grid points along the $x$ and $y$ directions. The result, shown in Fig. 2(b), confirms that the transferred charge is confined only to the $IrO_2$ planes, corroborating the impression gathered from the isosurface plot [Fig. 2(a)].

#### 3. Magnetism

We note that partially filling the narrow $J_{\text{eff}} = 1/2$ bands of Ir right above the Fermi level in Fig. 1(c) with the electrons transferred due to deposition of a polar oxide film in the presence of heavily tilted $IrO_6$ octahedra is expected to lead to interesting magnetic properties. Our calculations suggest that the Ir ions' magnetic moments are canted along the axes of the tilted $IrO_6$ octahedra. We have simulated three qualitatively different magnetic arrangements: (a) the canted ferromagnetic (FM) arrangement, where the canted magnetic moments point roughly along the same direction, (b) the canted checkerboard antiferromagnetic (CB-AFM) arrangement, where the second-nearest magnetic moments are in almost opposite directions, and (c) the canted striped antiferromagnetic (ST-AFM) arrangement, where nearly opposite magnetic moments form stripes. Our results for the projected magnetic moments and relative energies for different magnetic arrangements are tabulated in Table I. The results indicate that the canted CB-AFM is the most favored in terms of energy among the magnetic arrangements considered here. In addition to a substantial projected spin moment of $0.2\mu_B$, we observe a remarkably significant orbital moment of $0.24\mu_B$ projected onto the Ir ions, which may be attributed to Ir's strong spin-orbit interaction. We have also repeated the calculations with $U - J =$ 2 eV for Ir 5$d$ states and found qualitatively similar results with little increment in the projected magnetic moment (see Table I). The lowest-energy canted CB-AFM arrangement is depicted in the inset of Fig. 2(b) with arrows for the projected magnetic moment vectors. To assess the reliability of our results, we repeated the calculations within the local spin-density approximation + Hubbard $U$ method with a modest value of $U - J = 1.5$ eV for Ir 5$d$ states, considering spin-orbit coupling (LSDA + $U$ + SOC). The results reconfirm the canted CB-AFM as the lowest-energy state magnetic arrangement with $0.17\mu_B$ and $0.23\mu_B$ of projected spin and orbital moments, respectively, at Ir sites. The agreement of the results obtained within GGA + $U$ + SOC and LSDA + $U$ + SOC point to the robustness of our predictions for the magnetic properties of the heterostructure. The robust antiferromagnetism with substantial orbital moment makes the heterostructure promising for technologies based on antiferromagnetic spintronics.

#### 4. Rashba-like effect

Having an insight into the magnetic ground state of the LAO|SIO|STO heterostructure, we focus now on the consequences of a strong spin-orbit interaction of Ir 5$d$ electrons on the physical properties of the system. The results obtained from our electronic structure calculations for the heterostructure within GGA + $U$ + SOC are displayed in Fig. 3. We find from the band dispersion and DoS shown in Figs. 3(a) and 3(b), respectively, that the narrow (0.37 eV wide) Ir 5$d$ band above the Fermi energy highlighted in Fig. 1(c) gets broadened to ≈0.5 eV upon transfer of $0.5e^-$ per interface unit cell. The formation of the heterostructure and tilts of $IrO_6$ octahedra leads to broken symmetry that splits the Ir bands near the Fermi level, resulting in a dip in the DoS at the Fermi level. As a consequence of broken inversion symmetry in the presence of a microscopic electric field and a strong spin-orbit interaction, we expect to see a Rashba-like effect in the system that would separate the bands with different pseudospins in momentum space. Figure 3(c) displays the bands near the Fermi level along the $\bar{M} \rightarrow \Gamma \rightarrow M$ direction, confirming our expectation of Rashba-like split bands. To gain further insight into the electronic structure of these bands, we exploit the two-dimensional nature of the Brillouin zone for the heterostructure and plot the band energies as functions of $k_x$ and $k_y$, shown in Fig. 3(d). Examining Figs. 3(c) and 3(d), we observe the presence of electron pockets near the corners of the Brillouin zone and shallow hole pockets near the center of the Brillouin zone. The Fermi contours displayed in Fig. 3(e) confirm the location of the electron and hole pockets, while Fig. 3(f) reveals the shape of the hole pockets in three dimensions. A close look at the top of the bands highlighted in Fig. 3(g) reveals two peaks, which is not a characteristic of the Rashba effect alone. Furthermore, the constant-energy contours on the plane $E - E_F = 0.44$ eV [see Fig. 3(h)] exhibit double lines traced by nearly degenerate bands from different sublattices, a characteristic of constant-energy contours for Rashba-like split bands in an antiferromagnetic system [31], with elliptical arcs merging onto each other. These features call for a deeper understanding of the Rashba-like physics in the system.

#### 5. Anisotropic Rashba-Dresselhaus model

To better understand the unusual Rashba-like features of the system, we develop an analytical model of the anisotropic Rashba-Dresselhaus effect. The influence of an electric field along the $z$ direction on the electrons with strong spin-orbit interaction and structure inversion asymmetry (SIA) may be described by the Rashba Hamiltonian of the form [32]

$$H_R = \alpha(k_y\sigma_x - k_x\sigma_y), \tag{1}$$

where $\alpha$ is the Rashba coefficient, $k_x$ and $k_y$ are the components of crystal momentum, and $\sigma_x$ and $\sigma_y$ are the usual Pauli matrices. Similarly, the Dresselhaus Hamiltonian arising

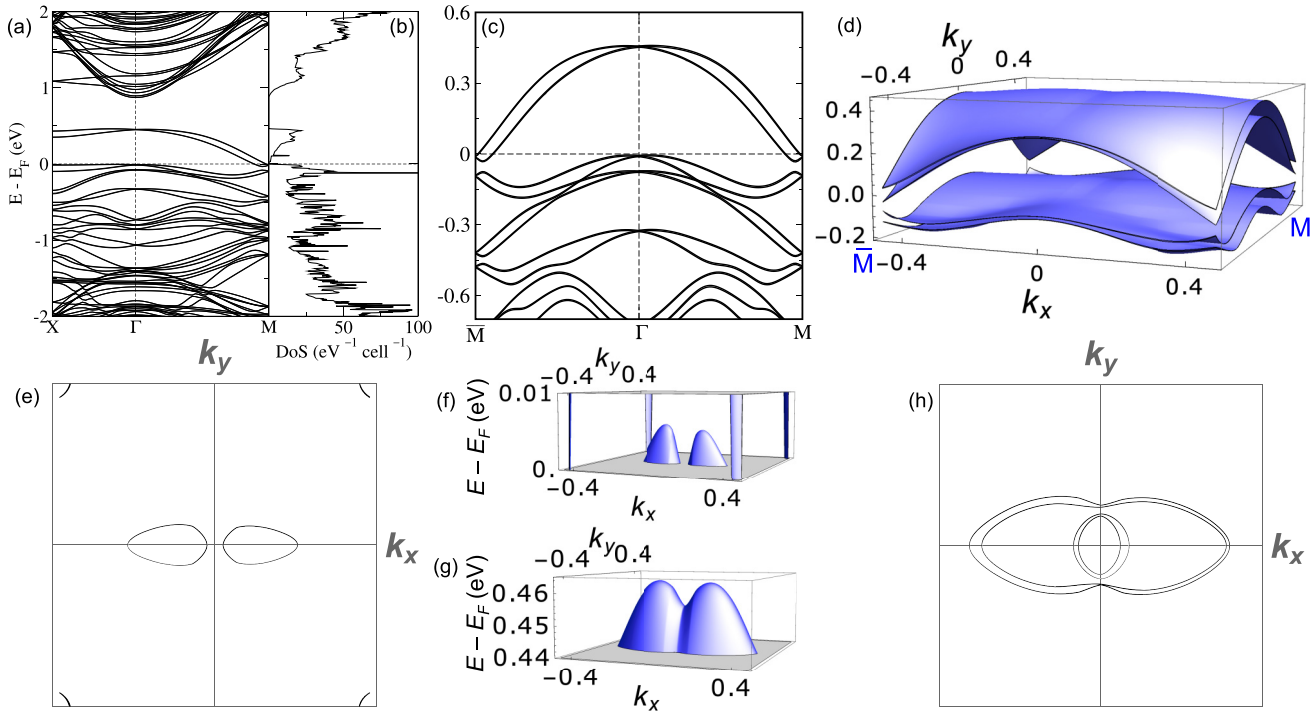


FIG. 3. The band dispersion of LAO|SIO|STO in the canted CB-AFM configuration along the high-symmetry directions $\mathrm{X} \to \Gamma \to \mathrm{M}$ and the density of states are shown in panels (a) and (b), respectively. Panel (c) shows the predominantly Ir $5d$ bands near the Fermi level along $\bar{\mathrm{M}} \to \Gamma \to \mathrm{M}$, highlighting the Rashba-like splitting. The bands touching the Fermi level have been plotted in three dimensions (3D) as functions of the crystal momenta $k_x$ and $k_y$, displayed in panel (d). The Fermi contours feature in panel (e), while the hole pockets are highlighted in a 3D plot, shown in panel (f). The top of the bands highlighted in panel (g) has two peaks, leading to double elliptical constant-energy contours on the plane $E - E_F = 0.44$ eV, shown in panel (h).

due to the spin-orbit interaction and bulk inversion asymmetry (BIA) is given as [33]

$$H_D = \beta(k_y\sigma_y - k_x\sigma_x), \tag{2}$$

with $\beta$ being the Dresselhaus coefficient. When treated as a perturbation to a free quasiparticle system with effective mass $m^*$, the Rashba (Dresselhaus) term leads to the eigenvalues

$$\varepsilon^{\pm}_{R(D)}(\vec{k}) = \frac{k^2}{2m^*} \pm \alpha(\beta)|\vec{k}|, \tag{3}$$

adjusting the units such that $\hbar = 1$. The qualitatively similar eigenvalues $\varepsilon^{\pm}_{R(D)}(\vec{k})$ from the Rashba and the Dresselhaus terms plotted as functions of $k_x$ and $k_y$ for $m^* < 0$ are shown in Fig. 4(a), while Fig. 4(b) displays a cross section of the same bands. Figure 4(c) displays the circular constant-energy contours, obtained by setting

$$\varepsilon^{\pm}_{R(D)}(\vec{k}) = \frac{k^2}{2m^*} \pm \alpha(\beta)|\vec{k}| = \text{constant}. \tag{4}$$

In the presence of both structure and bulk inversion asymmetry in a system, the combined Rashba-Dresselhaus Hamiltonian leads to the eigenvalues

$$\varepsilon^{\pm}_{RD}(\vec{k}) = \frac{k^2}{2m^*} \pm \sqrt{(\alpha^2+\beta^2)k^2 - 4\alpha\beta k_x k_y}, \tag{5}$$

featuring double-hill bands shown in Fig. 4(d) and a cross section in Fig. 4(e). While the double-hill pattern somewhat resembles the band structure obtained from our GGA + $U$ + SOC calculations [see Fig. 3(g)], the constant-energy contours in Fig. 4(f) exhibit significant differences with Fig. 3(h) in terms of shape and orientation—the former comprises circular arcs with a diagonal orientation, while the latter features elliptical arcs with an axial orientation. We note that the $a^0b^-c^-$ tilt pattern of the $IrO_6$ octahedra with no tilt about the $a$ axis and substantial tilt about the $b$ axis may lead to unequal quasiparticle effective masses along the $k_x$ and $k_y$ directions. Furthermore, we must increase the unit cell at least $\sqrt{2} \times \sqrt{2}$ times in the $ab$ plane in order to accommodate the $a^0b^-c^-$ tilt pattern (see Fig. 5), rotating the reciprocal cell by $\pi/4$ relative to the principal axes of effective mass. The transformed coordinates in the reciprocal space, $(K_X, K_Y)$, may be represented in terms of $(k_x, k_y)$ as

$$\begin{pmatrix} K_X \\ K_Y \end{pmatrix} = \frac{1}{\sqrt{2}} \begin{pmatrix} \cos\frac{\pi}{4} & \sin\frac{\pi}{4} \\ -\sin\frac{\pi}{4} & \cos\frac{\pi}{4} \end{pmatrix} \begin{pmatrix} k_x \\ k_y \end{pmatrix} = \frac{1}{2} \begin{pmatrix} k_x + k_y \\ k_y - k_x \end{pmatrix}. \tag{6}$$

Considering the anisotropic effective mass and the transformed reciprocal axes, we can write the Hamiltonian for the anisotropic Rashba-Dresselhaus model as

$$H_{ARD} = H_0 + \alpha(K_Y\sigma_x - K_X\sigma_y) + \beta(K_Y\sigma_y - K_X\sigma_x), \tag{7}$$

where

$$H_0 = -\frac{1}{2m^*_x}\frac{\partial^2}{\partial x^2} - \frac{1}{2m^*_y}\frac{\partial^2}{\partial y^2} \tag{8}$$

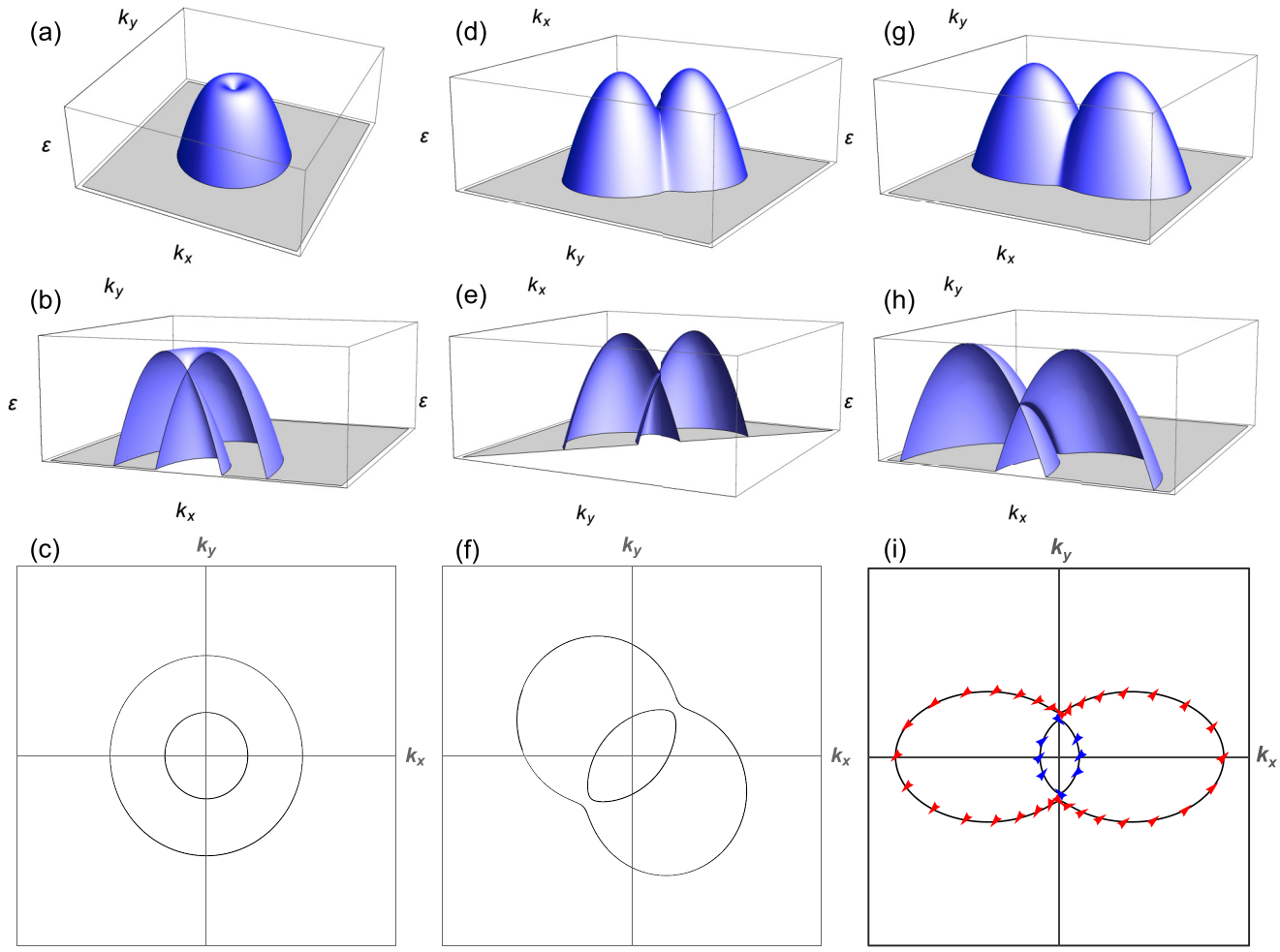


FIG. 4. We have shown the band dispersions $\varepsilon(\vec{k})$ and constant-energy contours obtained from our model calculations in this figure. Panels (a) and (b) show the dispersion for Rashba effect on isotropic bands, while panel (c) shows the corresponding constant-energy contours. Similarly, panels (d) and (e) show the band dispersion for a combination of isotropic Rashba and Dresselhaus effects, with the corresponding constant-energy contours in panel (f). Finally, the energy-momentum dispersion from our model for anisotropic Rashba-Dresselhaus effect with rotated Brillouin-zone features in panels (g) and (h), with the corresponding constant-energy contours in panel (i), marking the pseudospin directions with arrows.

is the kinetic energy term in two dimensions, with $m_x^*$ and $m_y^*$ representing the effective masses along $k_x$ and $k_y$, respectively. Treating the Rashba-Dresselhaus terms in Eq. (7) as perturbations to the free-electron-like Hamiltonian in Eq. (8) and using Eq. (6) for relating $(K_X, K_Y)$ to $(k_x, k_y)$, we evaluate the energy eigenvalues $\varepsilon^{\pm}_{ARD}(\vec{k})$ for the anisotropic Rashba-Dresselhaus system as

$$\varepsilon^{\pm}_{ARD}(\vec{k}) = \frac{k_x^2}{2m_x^*} + \frac{k_y^2}{2m_y^*} \pm \sqrt{2\left[(\alpha+\beta)^2 k_x^2 + (\alpha-\beta)^2 k_y^2\right]}. \tag{9}$$

Figures 4(g) and 4(h) show the double-hill bands and their cross section, respectively.

The constant-energy contours may be obtained in a polar coordinate system by putting $k_x = k\cos\phi$ and $k_y = k\sin\phi$, where $(k, \phi)$ are the usual polar coordinates,y and setting $\varepsilon^{\pm}_{ARD}$ in Eq. (9) to a constant $\varepsilon_c$, as below:

$$\begin{aligned}\varepsilon_c &= \frac{k^2\cos^2\phi}{2m_x^*} + \frac{k^2\sin^2\phi}{2m_y^*} \\ &\quad \pm \sqrt{2[(\alpha+\beta)^2 k^2\cos^2\phi + (\alpha-\beta)^2 k^2\sin^2\phi} \\ &= k^2\left(\frac{\cos^2\phi}{2m_x^*} + \frac{\sin^2\phi}{2m_y^*}\right) \pm k\sqrt{2(\alpha^2+\beta^2+2\alpha\beta\cos 2\phi)}.\end{aligned} \tag{10}$$

The roots of this quadratic equation give the constan-energy contours, as shown in Fig. 4(i), revealing no qualitative difference with our GGA + $U$ + SOC results [see Fig. 3(h)]. The model with the parameter values of $m_x^* = -0.81m_e$, $m_y^* = -0.29m_e$, $\alpha = 0.062$ eV Å, and $\beta = 0.044$ eV Å reasonably emulates our results from the GGA + $U$ + SOC calculations shown in Fig. 3(g), suggesting a large Rashba-Dresselhaus effect for the system—nearly two orders of magnitude greater than that of SIO|STO heterostructures [30]. Our estimated

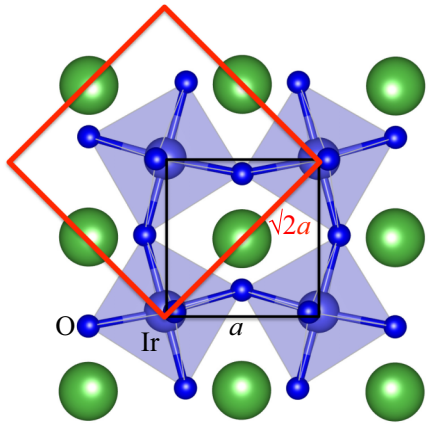


FIG. 5. The bigger (red) square represents the $\sqrt{2} \times \sqrt{2}$ times cell in the $ab$ plane that is required to accommodate the $IrO_6$ octahedra tilted in $a^0b^-c^-$ pattern, while the smaller (black) square shows the unit cell sufficient to describe the structure without octahedral tilts. They make an angle of $\pi/4$.

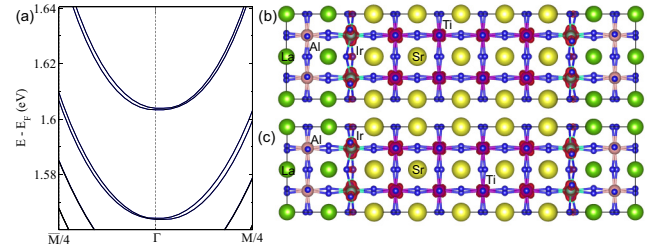


FIG. 6. Rashba-like effect for predominantly Ti $3d$ bands manifested due to proximity to strong spin-orbit entangled Ir are highlighted in panel (a). Panels (b) and (c) show the charge-density isosurfaces corresponding to upper and lower pairs of Rashba-like split bands in panel (a), respectively.

effective masses belong to a similar ballpark range as reported by Manca *et al.* [34] for the Ir $5d$ bands in the SIO|STO heterostructure, although with a different tilt pattern of the $IrO_6$ octahedra. Furthermore, anisotropic transport properties were reported in ultrathin SIO|STO heterostructures, in agreement with our model of anisotropic effective mass [35].

To visualize the pseudospin directions in the system, we evaluated the eigenstates $|\pm\rangle$ of the anisotropic Rashba-Dresselhaus Hamiltonian $H_{ARD}$ given in Eq. (7) as

$$|\pm\rangle = \frac{1}{\sqrt{2}}(\pm\zeta|\uparrow\rangle + |\downarrow\rangle), \tag{11}$$

where $|\uparrow\rangle$ and $|\downarrow\rangle$ are the eigenstates of the spin projection operator $S_z$, and

$$\zeta = \frac{(1-i)\sqrt{\alpha^2+\beta^2+2\alpha\beta\cos 2\phi}}{\sqrt{2}[(\alpha+\beta)\cos\phi + i(\alpha-\beta)\sin\phi]}, \quad \zeta^*\zeta = 1. \tag{12}$$

We may evaluate the expectation values of the spin-projections for $|\pm\rangle$ in the units of $\hbar$ as follows:

$$\begin{aligned}\langle S_z\rangle_+ &= \frac{1}{2}\langle+|\sigma_z|+\rangle = \frac{1}{4}(\zeta^*\zeta - 1) = 0 \\ &= \frac{1}{2}\langle-|\sigma_z|-\rangle = \langle S_z\rangle_-, \end{aligned} \tag{13}$$

$$\begin{aligned}\langle S_x\rangle_+ &= \frac{1}{2}\langle+|\sigma_x|+\rangle = \frac{1}{4}(\zeta+\zeta^*) \\ &= \frac{1}{2\sqrt{2}}\frac{(\alpha+\beta)\cos\phi - (\alpha-\beta)\sin\phi}{\sqrt{\alpha^2+\beta^2+2\alpha\beta\cos 2\phi}} \\ &= -\frac{1}{2}\langle-|\sigma_x|-\rangle = -\langle S_x\rangle_-, \end{aligned} \tag{14}$$

$$\begin{aligned}\langle S_y\rangle_+ &= \frac{1}{2}\langle+|\sigma_y|+\rangle = \frac{i}{4}(\zeta-\zeta^*) \\ &= \frac{1}{2\sqrt{2}}\frac{(\alpha+\beta)\cos\phi + (\alpha-\beta)\sin\phi}{\sqrt{\alpha^2+\beta^2+2\alpha\beta\cos 2\phi}} \\ &= -\frac{1}{2}\langle-|\sigma_y|-\rangle = -\langle S_y\rangle_-. \end{aligned} \tag{15}$$

The pseudospins obtained from Eqs. (13)–(15) is marked in Fig. 4(i), highlighting the rotation of the pseudospin direction.

The formation of electron and hole pockets hints that the number of charge carriers revealed in a transport measurement may be fewer than $0.5e^-$ per interface unit cell for this system. Nevertheless, the large Rashba-Dresselhaus effect observed here in conjunction with an antiferromagnetic ground state makes this heterostructure a lucrative material for emerging antiferromagnetic spintronics [1].

#### *6. Proximity effect*

After confirming a large Rashba-Dresselhaus effect from Ir $5d$ bands at the LAO|SIO|STO heterojunction, we carefully examine the empty Ti $3d$ states above the Fermi level. The relevant part of the band structure has been magnified and shown in Fig. 6(a), indicating much smaller, yet substantially Rashba-like split bands well above the Fermi level. Charge-density isosurfaces corresponding to the upper and the lower pair of Rashba-like split bands are depicted in Figs. 6(b) and 6(c), respectively, revealing predominant Ti $3d$ characters of the bands with some admixture of Ir $5d$ character. These Ti $3d$ bands visibly exhibit significantly more splitting than that of Ref. [36] for LAO|STO. This considerably larger Rashba-like splitting from Ti $3d$ bands can be attributed to the proximity to Ir $5d$ states with strong spin-orbit interaction.

## IV. DISCUSSION

The heterostructure of LAO|SIO|STO simulated here possesses a number of interesting properties at the ultrathin SIO layer, namely, (i) a two-dimensional conducting layer owing to charge transfer, (ii) broken inversion symmetry and a strong spin-orbit interaction driven anisotropic Rashba-Dresselhaus effect, (iii) canted antiferromagnetic order, and (iv) a proximity-driven Rashba-like effect. These properties make this heterostructure attractive for exploring antiferromagnetic spintronics. The strong anisotropic Rashba-Dresselhaus effect observed from our calculations in the two-dimensional conducting antiferromagnetic layer is promising for realizing spin-orbit torque. Furthermore, the robust insulating nature of STO and LAO with significant band gaps ensures that, except for the interface, the heterostructure remains insulating everywhere else, allowing for tuning the Rashba-Dresselhaus coefficients and the possible spin-orbit

torque via an external electric field or gate voltage over a wide range. Various spin textures may be realized in the noncollinear antiferromagnetic interface, which allows for storing and processing information, possibly at terahertz frequency and extremely low power, controlled via spin-orbit torque. Besides, the observation of an enhanced Rashba-like effect in Ti $3d$ states due to its proximity to Ir suggests opening up a new horizon in designing proximity-driven heterostructures for future technology. One of the advantages of proximity-induced spin-orbit interaction over adatom or substitution is that the host material's electronic structure is only slightly altered. Nevertheless, experimental verification of the predicted properties, such as the presence of a two-dimensional conducting layer, canted antiferromagnetism, and a strong anisotropic Rashba-Dresselhaus effect at the interface, and the hypothesized properties, such as tunable spin-orbit torque, are imperative for further progress.

## V. CONCLUSION

To conclude, we have simulated $SrIrO_3|SrTiO_3$ and $LaAlO_3|SrIrO_3|SrTiO_3$ heterostructures within the framework of density-functional theory including a Hubbard-$U$ correction and spin-orbit interactions. Our results suggest that the nonpolar $SrIrO_3|SrTiO_3$ heterostructure behaves like a canted antiferromagnetic Mott or Slater insulator with tilted $IrO_6$ octahedra. The polar|nonpolar heterostructure of $LaAlO_3|SrIrO_3|SrTiO_3$, where we assume one unit cell of $SrIrO_3$ sandwiched between a thin film of $LaAlO_3$ and a thick substrate of $SrTiO_3$, results in a two-dimensional conducting layer with electron and hole pockets at the interface $SrIrO_3$ unit cell. Our calculations reveal a canted antiferromagnetic ground state also for the $LaAlO_3|SrIrO_3|SrTiO_3$ heterostructure with tilted $IrO_6$ octahedra. We observe a strong anisotropic Rashba-Dresselhaus effect from the bands contributing to the conduction of charges. A physical model developed for the anisotropic Rashba-Dresselhaus effect without too many parameters nicely explains our results obtained from DFT $+ U +$ SOC calculations, providing rich physical insight into the system and illustrating pseudospin orientation. Based on these results, we hypothesize that electric-field-tunable spin-orbit torque may be realized at this heterojunction, making it an excellent test-bed for antiferromagnetic spintronics. Our predictions and hypotheses call for experimental verification for further progress in the field. In another crucial outcome, we find a pronounced Rashba-like effect at Ti $3d$ empty states because of its proximity to strong spin-orbit-coupled Ir atoms, provoking new designs of proximity-driven heterostructures for future technology.

## ACKNOWLEDGMENTS

Financial supports from SERB India through Grant No. ECR/2016/001004 and the use of the high-performance computing facility at IISER Bhopal are gratefully acknowledged.

## APPENDIX A: THE BRILLOUIN ZONE

The geometry of the Brillouin zone is important to understand the band dispersion of the heterostructures under consideration. Since we are interested in heterostructures of perovskite oxides where periodicity along the $c$ direction is unimportant, we can consider a two-dimensional (2D) Brillouin zone. A square lattice in the $ab$ plane would lead to a square-shaped Brillouin zone, as shown in Fig. 7. The zone boundary is marked with thick red lines, and the momentum axes $k_x$ and $k_y$ are marked with black lines. The high-symmetry points along with their coordinates are marked on the figure. It is customary to represent the coordinates in the Brillouin zone in units of $2\pi/a$, transforming the coordinates of the $X$ point into $(0.5, 0)$, the coordinates of the $M$ point into $(0.5, 0.5)$, and so on. A combination of inversion symmetry and fourfold rotational symmetry transforms the irreducible part of the Brillouin zone into a triangle with $X$, $\Gamma$, and $M$ points at the corners. However, the systems considered

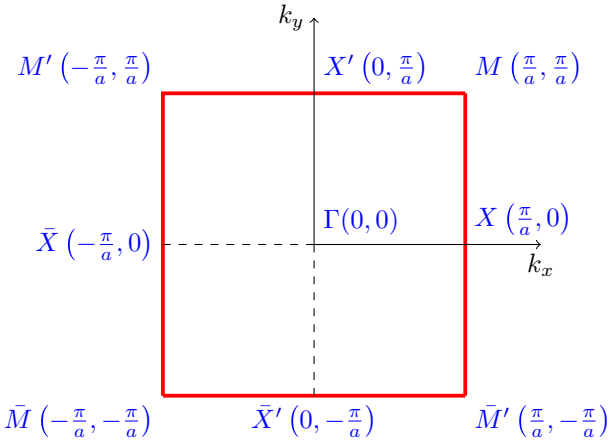


FIG. 7. A two-dimensional Brillouin zone of square shape is depicted here. The relevant high-symmetry points, i.e., the $\Gamma$ point, four $X$ equivalent points, and four $M$ equivalent points along with their coordinates are marked in the figure.

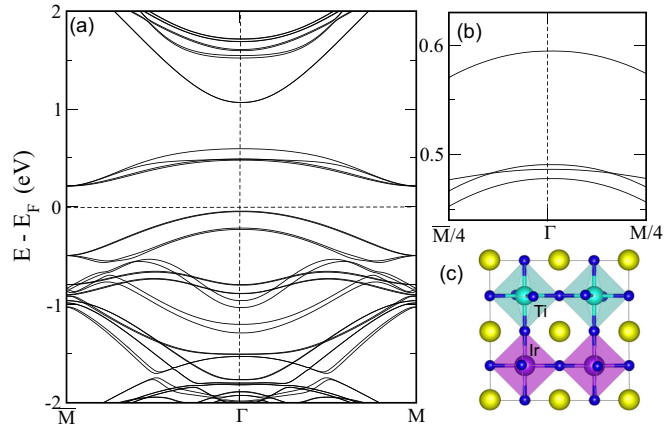


FIG. 8. Panel (a) shows the band structure of the $(SrIrO_3)_1|(SrTiO_3)_1$ heterostructure along $\bar{M} \to \Gamma \to M$, while panel (b) zooms in on the Ir $5d$ bands above the Fermi level, revealing no signature of Rashba-like effect. Panel (c) depicts the structure of $SrIrO_3|SrTiO_3$ as viewed from the $a$ axis, revealing the absence of tilt about the $a$ axis.

here do not obey any of these symmetries, making the entire Brillouin zone irreducible. The effective 2D nature of the Brillouin zone allows for the band dispersion $\varepsilon(\vec{k})$, $\vec{k} = (k_x, k_y)$ being adequately represented in a 3D figure. Furthermore, the Fermi surface (constant-energy surface) reduces to Fermi contours (constant-energy contours) in this context.

## APPENDIX B: NO SIGNATURE OF RASHBA EFFECT IN $SrIrO_3|SrTiO_3$ HETEROSTRUCTURE

As discussed earlier, an electric field is generated in the heterostructure due to the deposition of a polar perovskite oxide thin film of $LaAlO_3$. The electrostatics of heterostructuring a polar and a nonpolar perovskite oxide has been discussed in detail in Ref. [15]. We aim at understanding the role of this electric field in the Rashba-like effect. Therefore, we carefully examine the band structure of the $SrIrO_3|SrTiO_3$ heterostructure calculated within the GGA + $U$ + SOC method in the absence of the polar $LaAlO_3$ thin film. Our results, shown in Fig. 8(a), display the bands along $\bar{\mathrm{M}} \rightarrow \Gamma \rightarrow \mathrm{M}$ direction, while Fig. 8(b) zooms in on the Ir 5$d$ bands right above the Fermi level to highlight any Rashba-like effect. We hardly observe any Rashba-like effect for this heterostructure, consistent with an experimental report of a weak, temperature-dependent Rashba-like effect [30], seemingly because of the absence of any microscopic electric field. However, an externally applied electric field along the $c$ direction may introduce a substantial Rashba-like effect in this system, owing to the spin-orbit entangled Ir 5$d$ states. Such an electric field may also transform the heterostructure into a conducting one.


[1] V. Baltz, A. Manchon, M. Tsoi, T. Moriyama, T. Ono, and Y. Tserkovnyak, Antiferromagnetic spintronics, Rev. Mod. Phys. **90**, 015005 (2018).

[2] J. Železný, P. Wadley, K. Olejník, A. Hoffmann, and H. Ohno, Spin transport and spin torque in antiferromagnetic devices, Nat. Phys. **14**, 220 (2018).

[3] O. Gomonay, V. Baltz, A. Brataas, and Y. Tserkovnyak, Antiferromagnetic spin textures and dynamics, Nat. Phys. **14**, 213 (2018).

[4] T. Jungwirth, X. Marti, P. Wadley, and J. Wunderlich, Antiferromagnetic spintronics, Nat. Nanotechnol. **11**, 231 (2016).

[5] K. Olejník, T. Seifert, Z. Kašpar, V. Novák, P. Wadley, R. P. Campion, M. Baumgartner, P. Gambardella, P. Němec, J. Wunderlich, J. Sinova, P. Kužel, M. Müller, T. Kampfrath, and T. Jungwirth, Terahertz electrical writing speed in an antiferromagnetic memory, Sci. Adv. **4**, eaar3566 (2018).

[6] B. J. Kim, H. Jin, S. J. Moon, J.-Y. Kim, B.-G. Park, C. S. Leem, J. Yu, T. W. Noh, C. Kim, S.-J. Oh, J.-H. Park, V. Durairaj, G. Cao, and E. Rotenberg, Novel $J_{\mathrm{eff}} = 1/2$ Mott State Induced by Relativistic Spin-Orbit Coupling in $Sr_2IrO_4$, Phys. Rev. Lett. **101**, 076402 (2008).

[7] K. A. Modic, T. E. Smidt, I. Kimchi, N. P. Breznay, A. Biffin, S. Choi, R. D. Johnson, R. Coldea, P. Watkins-Curry, G. T. McCandless, J. Y. Chan, F. Gandara, Z. Islam, A. Vishwanath, A. Shekhter, R. D. McDonald, and J. G. Analytis, Realization of a three-dimensional spin-anisotropic harmonic honeycomb iridate, Nat. Commun. **5**, 4203 (2014).

[8] J. Chakraborty, Interplay of covalency, spin-orbit coupling, and geometric frustration in the $d^{3.5}$ system $Ba_3LiIr_2O_9$, Phys. Rev. B **97**, 235147 (2018).

[9] J. Matsuno, K. Ihara, S. Yamamura, H. Wadati, K. Ishii, V. V. Shankar, H.-Y. Kee, and H. Takagi, Engineering a Spin-Orbital Magnetic Insulator by Tailoring Superlattices, Phys. Rev. Lett. **114**, 247209 (2015).

[10] D. J. Groenendijk, C. Autieri, J. Girovsky, M. C. Martinez-Velarte, N. Manca, G. Mattoni, A. M. R. V. L. Monteiro, N. Gauquelin, J. Verbeeck, A. F. Otte, M. Gabay, S. Picozzi, and A. D. Caviglia, Spin-Orbit Semimetal $SrIrO_3$ in the Two-Dimensional Limit, Phys. Rev. Lett. **119**, 256403 (2017).

[11] Y. Ohuchi, J. Matsuno, N. Ogawa, Y. Kozuka, M. Uchida, Y. Tokura, and M. Kawasaki, Electric-field control of anomalous and topological Hall effects in oxide bilayer thin films, Nat. Commun. **9**, 213 (2018).

[12] C. Bhandari and S. Satpathy, Spin-orbital entangled two-dimensional electron gas at the $LaAlO_3/Sr_2IrO_4$ interface, Phys. Rev. B **98**, 041303(R) (2018).

[13] A. S. Everhardt, M. DC, X. Huang, S. Sayed, T. A. Gosavi, Y. Tang, C.-C. Lin, S. Manipatruni, I. A. Young, S. Datta, J.-P. Wang, and R. Ramesh, Tunable charge to spin conversion in strontium iridate thin films, Phys. Rev. Mater. **3**, 051201 (2019).

[14] H. Wang, K.-Y. Meng, P. Zhang, J. T. Hou, J. Finley, J. Han, F. Yang, and L. Liu, Large spin-orbit torque observed in epitaxial $SrIrO_3$ thin films, Appl. Phys. Lett. **114**, 232406 (2019).

[15] N. Ganguli and P. J. Kelly, Tuning Ferromagnetism at Interfaces between Insulating Perovskite Oxides, Phys. Rev. Lett. **113**, 127201 (2014).

[16] P. E. Blöchl, Projector augmented-wave method, Phys. Rev. B **50**, 17953 (1994).

[17] G. Kresse and J. Hafner, *Ab initio* molecular dynamics for liquid metals, Phys. Rev. B **47**, 558 (1993).

[18] G. Kresse and D. Joubert, From ultrasoft pseudopotentials to the projector augmented-wave method, Phys. Rev. B **59**, 1758 (1999).

[19] J. P. Perdew, K. Burke, and M. Ernzerhof, Generalized Gradient Approximation Made Simple, Phys. Rev. Lett. **77**, 3865 (1996).

[20] D. M. Ceperley and B. J. Alder, Ground State of the Electron Gas by a Stochastic Method, Phys. Rev. Lett. **45**, 566 (1980).

[21] J. P. Perdew and A. Zunger, Self-interaction correction to density-functional approximations for many-electron systems, Phys. Rev. B **23**, 5048 (1981).

[22] S. L. Dudarev, G. A. Botton, S. Y. Savrasov, C. J. Humphreys, and A. P. Sutton, Electron-energy-loss spectra and the structural stability of nickel oxide: An LSDA + U study, Phys. Rev. B **57**, 1505 (1998).

[23] P. E. Blöchl, O. Jepsen, and O. K. Andersen, Improved tetrahedron method for Brillouin-zone integrations, Phys. Rev. B **49**, 16223 (1994).

[24] A. M. Glazer, The classification of tilted octahedra in perovskites, Acta Crystallogr., Sect. B: Struct. Crystallogr. Cryst. Chem. **28**, 3384 (1972).

[25] A. Biswas, K.-S. Kim, and Y. H. Jeong, Metal insulator transitions in perovskite $SrIrO_3$ thin films, J. Appl. Phys. **116**, 213704 (2014).

[26] J. H. Gruenewald, J. Nichols, J. Terzic, G. Cao, J. W. Brill, and S. S. Seo, Compressive strain-induced metal-insulator transition in orthorhombic $SrIrO_3$ thin films, J. Mater. Res. **29**, 2491 (2014).

[27] W. Fan and S. Yunoki, Electronic and magnetic structure under lattice distortion in $SrIrO_3/SrTiO_3$ superlattice: A first-principles study, J. Phys.: Conf. Ser. **592**, 012139 (2015).

[28] H. Watanabe, T. Shirakawa, and S. Yunoki, Theoretical study of insulating mechanism in multiorbital Hubbard models with a large spin-orbit coupling: Slater versus Mott scenario in $Sr_2IrO_4$, Phys. Rev. B **89**, 165115 (2014).

[29] P. Schütz, D. Di Sante, L. Dudy, J. Gabel, M. Stübinger, M. Kamp, Y. Huang, M. Capone, M.-A. Husanu, V. N. Strocov, G. Sangiovanni, M. Sing, and R. Claessen, Dimensionality-Driven Metal-Insulator Transition in Spin-Orbit-Coupled $SrIrO_3$, Phys. Rev. Lett. **119**, 256404 (2017).

[30] L. Zhang, Y. B. Chen, B. Zhang, J. Zhou, S. Zhang, Z. Gu, S. Yao, and Y. Chen, Sensitively temperature-dependent spin-orbit coupling in $SrIrO_3$ thin films, J. Phys. Soc. Jpn. **83**, 054707 (2014).

[31] O. Krupin, G. Bihlmayer, K. M. Döbrich, J. E. Prieto, K. Starke, S. Gorovikov, S. Blügel, S. Kevan, and G. Kaindl, Rashba effect at the surfaces of rare-earth metals and their monoxides, New J. Phys. **11**, 013035 (2009).

[32] E. I. Rashba, Properties of semiconductors with an extremum loop. 1. Cyclotron and combinational resonance in a magnetic field perpendicular to the plane of the loop, Sov. Phys. Solid State **2**, 1109 (1960).

[33] G. Dresselhaus, Spin-orbit coupling effects in zinc blende structures, Phys. Rev. **100**, 580 (1955).

[34] N. Manca, D. J. Groenendijk, I. Pallecchi, C. Autieri, L. M. Tang, F. Telesio, G. Mattoni, A. McCollam, S. Picozzi, and A. D. Caviglia, Balanced electron-hole transport in spin-orbit semimetal $SrIrO_3$ heterostructures, Phys. Rev. B **97**, 081105(R) (2018).

[35] T. C. van Thiel, J. Fowlie, C. Autieri, N. Manca, M. Šiškins, D. Afanasiev, S. Gariglio, and A. D. Caviglia, Coupling lattice instabilities across the interface in ultrathin oxide heterostructures, ACS Materials Letters **2**, 389 (2020).

[36] Z. Zhong, A. Tóth, and K. Held, Theory of spin-orbit coupling at $LaAlO_3/SrTiO_3$ interfaces and $SrTiO_3$ surfaces, Phys. Rev. B **87**, 161102(R) (2013).